




***Ab initio* study of pressure-induced structural and electronic phase transitions in Ca_2RuO_4** Harry D. J. Keen ¹, Stephen R. Julian ², and Andreas Hermann ¹¹*School of Physics and Astronomy, University of Edinburgh, Edinburgh EH9 3FD, United Kingdom*²*Department of Physics, University of Toronto, Toronto, ON M5S 1A1, Canada*

(Received 9 July 2020; revised 21 July 2021; accepted 12 August 2021; published 23 August 2021)

Ca_2RuO_4 is a compound with a Mott insulating ground state, which responds to external pressure in a variety of ways, some of which are expected (an insulator-metal transition) while others are more surprising (an expansion of the c lattice constant). We provide here a comprehensive study of these pressure-induced structural and electronic changes using DFT+ U calculations, and demonstrate generally good agreement with experiment. The insulator-metal transition is reproduced and coincides with an isostructural transition, the c lattice expansion, RuO_6 octahedral distortions, and associated changes to the Ru $4d$ orbital order. The metallic part of the phase diagram features several competing phases. The high-pressure $Bbcm$ phase is found to be unstable in the ground state over a broad pressure range and suggested to be thermally stabilized instead.

DOI: [10.1103/PhysRevB.104.085143](https://doi.org/10.1103/PhysRevB.104.085143)

Ca_2RuO_4 is a layered perovskite compound with a rich phase diagram, featuring a metal-insulator transition with a structural distortion upon cooling, antiferromagnetic ordering upon further cooling, and metallization and ferromagnetic order, followed by a further structural transition, under pressure [1–3]. It is one end member of the $\text{Ca}_{2-x}\text{Sr}_x\text{RuO}_4$ series that includes the unconventional superconductor Sr_2RuO_4 at the other end [4,5]. Ca_2RuO_4 shows intriguing collective phenomena in its own right, such as pressure-driven superconductivity, electric-field-induced metallization, negative thermal expansion, and a Higgs mode [6–9]. Several of these properties are intricately linked to structural distortions of the RuO_6 octahedra, which in turn can be controlled by applying hydrostatic pressure [2,3] or uniaxial strain [10,11].

High-pressure resistivity and x-ray and neutron diffraction measurements of Ca_2RuO_4 have been reported [2,3]. At 0.5 GPa at room temperature Ca_2RuO_4 undergoes a Mott insulator-metal transition [2], which is accompanied by a simultaneous first-order structural transition [3] that retains the same orthorhombic symmetry. The transition pressure is insensitive to cooling [2]. The low pressure insulating phase is referred to as $S\text{-}Pbca$ (with a “short” c axis) and the high pressure metallic phase as $L\text{-}Pbca$ (with a “long” c axis, this is also the high-temperature ambient pressure phase). The metallic $L\text{-}Pbca$ phase is a two-dimensional, itinerant ferromagnet [2]. Upon pressure increase both $S\text{-}$ and $L\text{-}Pbca$ show rather peculiar structural behavior: an expansion of the c lattice constant as a function of pressure, i.e., $\partial c/\partial P > 0$ [3]. This behavior persists until a second-order structural phase transition from $L\text{-}Pbca$ to a higher symmetry $Bbcm$ phase at 5.5 GPa, which marks a maximum in c . Within the $Bbcm$ phase the c axis returns to conventional behavior; $\partial c/\partial P < 0$. In the transition from $L\text{-}Pbca$ to $Bbcm$ the octahedral tilt against the c axis vanishes, while the system remains metallic. This sequence of structural and electronic changes remains unexplored from an *ab initio* perspective.

At ambient conditions, the electronic structure of Ca_2RuO_4 has been explored in several computational studies, which typically combine density functional (DFT) and dynamical mean field theory to capture the dominant Mott insulator physics, and tend to focus largely on magnetic degrees of freedom [12–21]. However, these studies have all used experimental lattice parameters (in some cases interpolations between $S\text{-}$ and $L\text{-}Pbca$ or along the Ca-Sr composition axis) and almost all bypass the relative energies of the different structures. While there is recognition that the Mott transition in Ca_2RuO_4 correlates with structural changes [18–20], pressure effects have only very recently been modeled, in a Landau-Ginzburg free energy expansion of the ambient pressure structures [20] and dynamical mean field theory applied to experimental high-pressure structures [21].

In this paper we study the high-pressure phase evolution of Ca_2RuO_4 using DFT and DFT+ U calculations. We consider a range of on-site repulsion terms U in order to reflect the expected sensitivity of U to pressure. All presented structures are fully self-consistent, with simultaneously optimised electron density and crystal structure. We reproduce the first-order structural phase transition and show that it coincides with the insulator-metal transition. We also find that the c lattice expansion under pressure in the $S\text{-}Pbca$ and (to some extent) $L\text{-}Pbca$ phases correlates with octahedral distortions and changes in the Ru $4d$ occupancies, reaffirming the intimate connection between electronic and structural degrees of freedom in Ca_2RuO_4 . While the insulating $S\text{-}Pbca$ phase is robust in our calculations, we find several different metallic $Pbca$ ground state phases, indicating a complex energetic landscape in the metallic region of the phase diagram.

I. COMPUTATIONAL METHOD

DFT calculations are carried out using the Vienna *ab initio* simulation package (VASP) [22] using the Perdew, Burke, and Ernzerhof (PBE) exchange-correlation functional [23] in

conjunction with a plane wave basis (cutoff energy $E_c = 500$ eV) and the projector augmented wave method [24]. Tests with the LDA and SCAN functionals [25,26] revealed qualitatively similar results (see the Supplemental Material (SM) for details [27]). Brillouin zones are sampled using regular $8 \times 8 \times 4$ k -point grids. All lattice vectors and atomic positions are fully optimized at all pressures, and considered converged once all force components are smaller than 1 meV/Å. The inclusion of spin-orbit coupling (SOC) is prohibitively expensive for the number of calculations we present here. In addition, our tests at zero pressure show that SOC does not significantly influence the results (see the SM [27]), so it is omitted here.

Magnetism is an important ingredient for enforcing a realistic orbital structure on the Ru sites, which is in turn intimately connected to the octahedral distortions. In fact, the failure to include magnetism can induce spurious structural and electronic properties (see the SM [27]). However, correlation between Ru moments should have little influence on the crystal structure, so for all calculations presented here we use a uniform ferromagnetic state with moments along c . The effect of single-ion anisotropy (which forces moments to lie roughly in the ab plane in experiment) relies on the inclusion of SOC [3], so it is a small effect which we neglect here.

The treatment of Coulomb interactions between localized states in DFT is insufficient to capture the Mott localization of the Ru $4d$ electrons that controls the physics of Ca_2RuO_4 . The only available approach for correcting the overdelocalization of these states that also allows for structural relaxation under pressure is the DFT+ U method [32]. For our calculations we use the simplified formalism by Dudarev [33] with a single effective parameter U (sometimes referred to as $U_{\text{eff}} = U - J$ in the literature).

The pressure dependence of U is not straightforward. As the application of pressure is expected to delocalize electrons, the failures of DFT should become less severe under compression. From a DFT+ U perspective, increasing pressure should thus be accompanied by a corresponding decrease in the correction U . In this work the precise pressure dependence of U is not pursued. Instead, all calculations are performed for a range of U values in the vicinity of the Mott transition. Qualitatively, the complete picture will be an interpolation from results at large U at low pressures to the results at small U for high pressures.

II. RESULTS

The results of our calculations are presented as follows: In Sec. II A the U dependence of Ca_2RuO_4 is probed at zero pressure. The phase diagram in (P, U) space is presented in Sec. II B where pressure driven phase transitions are identified with reference to crystal structures and the electronic density of states (DOS). In Secs. II C and II D, respectively, the octahedral distortions and Ru $4d$ orbital structure are examined more closely to identify signatures of the pressure driven phase transitions. Finally, in Sec. II E the stability of the high symmetry $Bbcm$ phase is considered with reference to the relaxed $Pbca$ structures at high pressure.

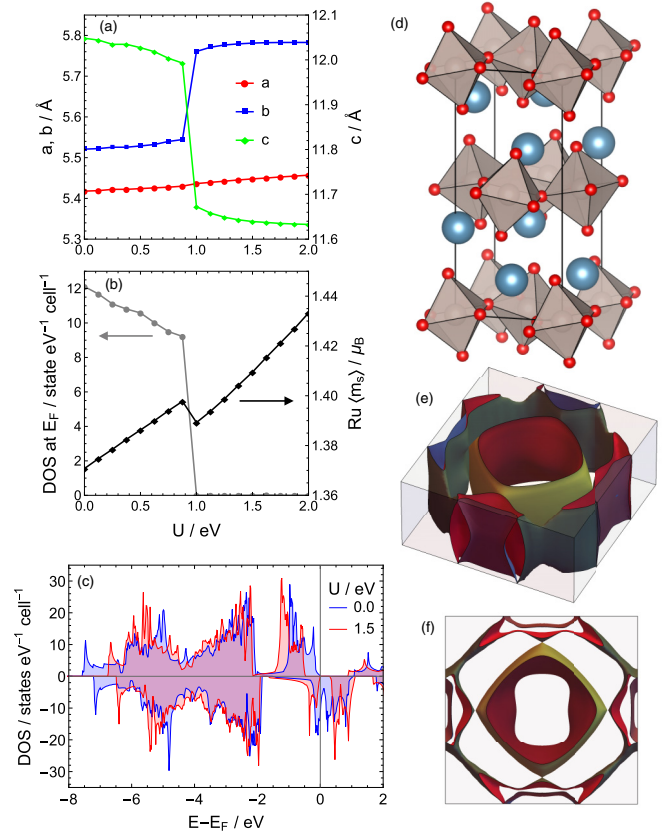


FIG. 1. (a) Optimized lattice parameters of Ca_2RuO_4 at atmospheric pressure as function of U . Left axis is for a and b , right axis for c . (b) DOS at the Fermi energy (left axis) and average Ru spin moment (right axis) as a function of U at atmospheric pressure. (c) Spin-resolved DOS near the Fermi energy for $U = 0.0$ eV (a half-metallic phase) and $U = 1.5$ eV (an insulating phase). (d) The experimental S - $Pbca$ crystal structure. Blue spheres are Ca, brown polyhedra are the RuO_6 octahedra. (e) The Fermi surface for $U = 0.0$ eV. (f) The Fermi surface viewed along k_z .

A. Atmospheric pressure

DFT, without any corrections for strong Coulomb interactions, incorrectly predicts that Ca_2RuO_4 is a metal at atmospheric pressure. The addition of the on-site U term is sufficient to correct this. Figure 1 shows the U dependence of the crystal and electronic structure. For $U < 1$ eV the system relaxes into a half-metallic state with $c \sim 12.05$ Å. This is somewhat shorter than the experimental measurements of the metallic L - $Pbca$ phase, which are $c = 12.26$ Å at 400 K and atmospheric pressure [34], and $c = 12.29$ Å at 295 K and 1 GPa [3]. While the Fermi surface is largely two dimensional [Figs. 1(e) and 1(f)], this half-metallic phase also has a large spin moment of $1.4 \mu_B$, which is inconsistent with the small itinerant moment of $\sim 0.4 \mu_B$ seen in the L - $Pbca$ phase [2,3]. For $U \geq 1.0$ eV the system relaxes into an insulating phase where the c axis drastically shortens and the difference between the a and b axes increases. This is accompanied by a reduced bandwidth and a gap opening in the spin-minority DOS. The lattice parameters of this phase are broadly consistent with the insulating S - $Pbca$ phase at low temperature measured by Porter *et al.* [34], albeit with a slightly

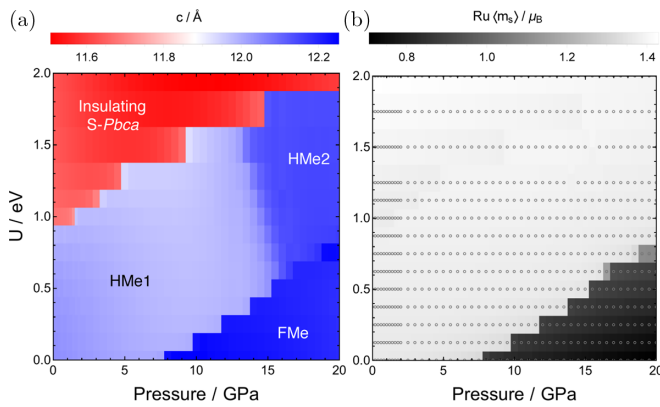


FIG. 2. (a) Phase diagram of the Ca_2RuO_4 ground state in (P, U) space, based on analysis of $Pbca$ structures. Four phases are identified: insulating $S\text{-}Pbca$, half-metallic $Pbca\text{-}1$ (HMe1), half-metallic $Pbca\text{-}2$ (HMe2), and a fully metallic $Pbca$ (FMe). Color scale indicates the length of the c axis. (b): The magnitude of the Ru spin moment in (P, U) space. Overlaid points show the grid of calculations used to build both diagrams.

exaggerated difference between a and b . The large moment size of $1.4 \mu_B$ persists in this insulating phase, consistent with experiment [3].

B. Pressure-induced $Pbca$ transitions

The optimized structures at atmospheric pressure serve as a starting point for our calculations under pressure. For a selection of U , these structures are compressed up to an external pressure of 20 GPa; first in steps of 0.2 up to 2 GPa, then in steps of 0.5 GPa. Each calculation starts from the optimized structure at the preceding pressure. In this section we present the lattice vectors and classify structures based on the DOS; the more subtle structural features of the octahedra are discussed in Sec. II C.

Figure 2 shows the main result as a phase diagram in (P, U) space. The insulating $S\text{-}Pbca$ phase becomes less stable under compression, and a pressure-driven phase transition to the half-metallic phase (HMe1) appears. With increased pressure the landscape becomes more complex as new metallic phases appear. For small U , a fully metallic phase (FMe) appears with a longer c axis and much smaller moment of $\sim 0.8 \mu_B$, much closer to experiment and indicative of itinerant electron magnetism. For larger U , this is replaced by a second half-metallic phase (HMe2) with an intermediate c -axis length. The Fermi surfaces and DOS's of these two new metallic phases are shown in Fig. 3. Compared to the first HMe1 (as shown in Fig. 1 and discussed in the previous section), both of these structures have much larger bandwidths. For smaller U , where on-site Coulomb interactions are energetically less penalizing, both spin channels cross the Fermi energy and a smaller total moment is stabilized. For larger U , the cost of double occupancy in the Ru $4d$ states is too severe, and thus the large moment and half-metallicity is preserved. The Fermi surfaces show that both high-pressure metals HMe2 and FMe are more two dimensional than HMe1, and have promising support for nesting vectors.

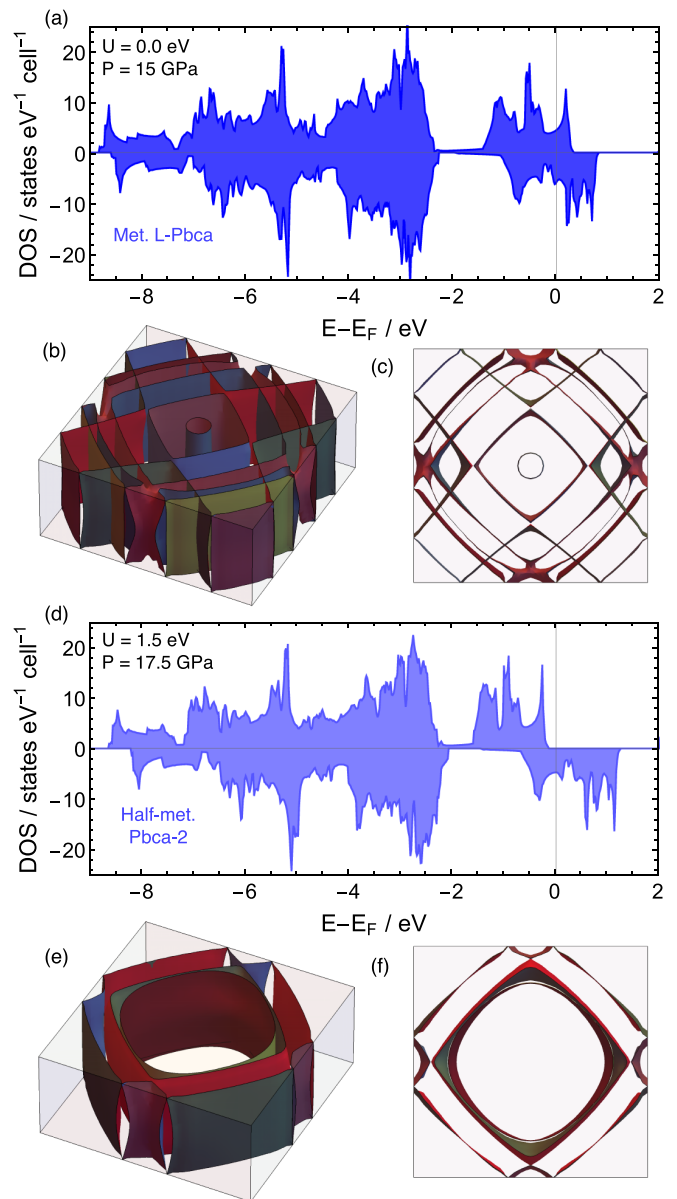


FIG. 3. (a) DOS of the FMe phase at $P = 15$ GPa for $U = 0.0$ eV. (b) The corresponding Fermi surface and (c) the Fermi surface viewed along k_z . (d)–(f) The same for the HMe2 phase at $P = 17.5$ GPa for $U = 1.5$ eV.

The consequences of these transitions on the lattice parameters are shown in Fig. 4, compared with experimental data. Despite the $S \rightarrow L$ transition being sharply first order, the $S\text{-}Pbca$ phase shows a smooth upturn in the c lattice constant prior to the transition pressure, reproducing the c axis increase seen in experiment. Of the metallic phases on offer, the FMe phase offers the best agreement with experiment in both the length of the c axis, and in predicting that $a \approx b$. However, it does not show an increase of the c axis $\partial c / \partial P > 0$, whereas the boundary between the two half-metallic phases does. Nevertheless, the experimental data for the c axis in the $L\text{-}Pbca$ phase is rather noisy. This may be indicative of the complex energetic landscape that the metallic phase navigates, and the positive slope a result of the imminent $Bbcm$ phase.

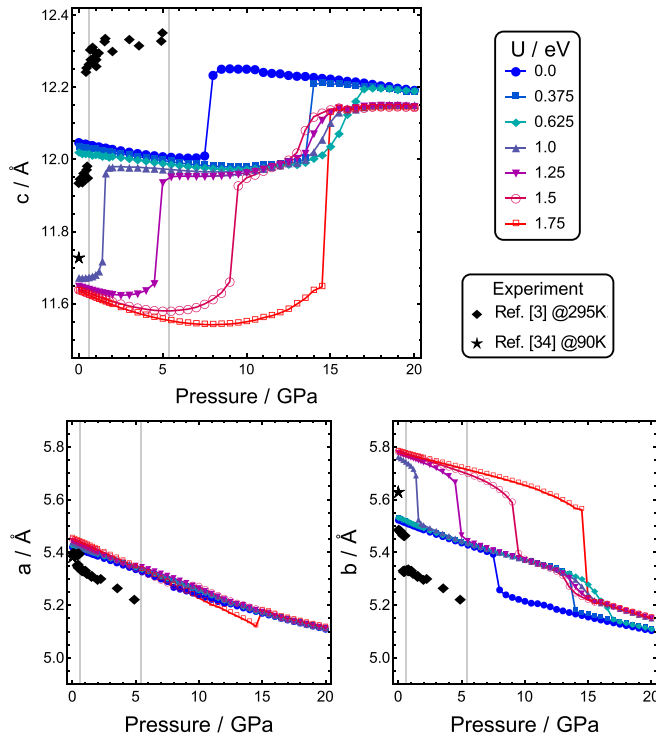


FIG. 4. Pressure dependence of the lattice parameters for a range of representative U values. Experimental data at two different temperatures are marked by filled black symbols, and vertical lines indicate the pressure-driven structural phase transitions identified in experiment at 295 K by Steffens *et al.* [3]. For clarity, only the experimental data in the $Pbca$ phases are shown [3,34].

The insulator-metal transition pressure is extremely sensitive to changes in U . The experimental transition pressure is 0.5 GPa at room temperature [3], and remains unchanged at much lower temperatures [2]. This suggests that $U \lesssim 1.0$ eV is appropriate for modeling the $S-Pbca$ phase. Furthermore, for any comparisons it is important to appreciate the significant temperature dependence of the Ca_2RuO_4 crystal structure. Low-temperature structural data exists only at ambient pressure [34] and is included in Fig. 4. Within the $S-Pbca$ phase, the c lattice constant expands with increased temperature, while b contracts (both with coefficients $\alpha \approx \pm 10^{-4} \text{ K}^{-1}$) and a remains constant. Our ground state results for $U \geq 1.0$ eV are therefore in good agreement with experimental data on the $S-Pbca$ phase. For $L-Pbca$, comparisons are further complicated by lack of thermal expansivity data at high pressure. Figure 4 implies that the FMe phase stabilized with $U = 0.0$ eV at high pressure, gives the best agreement with experiment. This is not necessarily in contradiction with the $S-Pbca$ results: one should not expect that a constant value of U is sufficient for all phases. The discontinuous change in crystal and electronic structure will result in a discontinuous change in the effective U required to model the metallic phase. Specifically, U should decrease after the phase transition, which puts the system much closer to the more physical FMe phase.

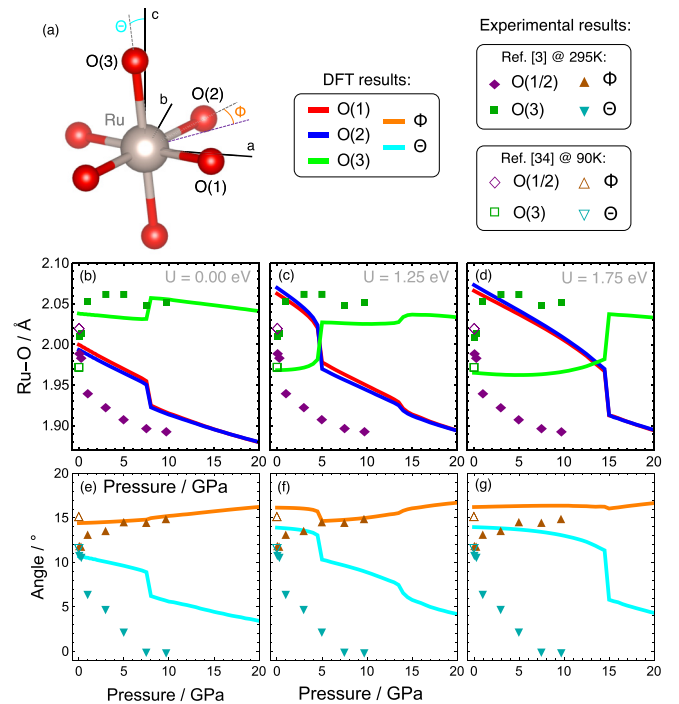


FIG. 5. (a) Labeling convention for O sites and distortion angles in RuO_6 . Purple dashed line is the [110] direction. Θ and Φ are the tilt and rotation angles, respectively. (b)–(g) Octahedral bond lengths and distortion angles as a function of pressure for $U = 0.0, 1.25,$ and 1.75 eV.

C. Octahedral distortion under pressure

The pressure dependence of perovskitelike materials is usually adequately captured by rotations and tilts of rigid octahedra [35–37]. For instance, in Steffens *et al.*'s analysis of Ca_2RuO_4 it was assumed that the octahedral basal plane Ru-O bonds remained equal and perpendicular [3]. However, polyhedral plasticity has been identified as a catalyst for unexpected structural behavior in SrRuO_3 and coupling to electronic transitions in rare earth nickelates RENiO_3 [38–42]. We therefore investigate the geometry of the RuO_6 octahedra in Ca_2RuO_4 in more detail here.

To capture the different high-pressure scenarios identified in the previous section, we select three exemplar values of U . These are $U = 0.0$ eV (HMe1 \rightarrow FMe), $U = 1.25$ eV (ins. $S-Pbca \rightarrow$ HMe1 \rightarrow HMe2) and $U = 1.75$ eV (ins. $S-Pbca \rightarrow$ HMe2), which covers all pressure-induced phase transitions seen in DFT+ U . Figures 5(b)–5(g) show the pressure dependencies of the octahedral Ru-O bond lengths and distortion angles. The labeling conventions for these parameters are given in Fig. 5(a). The Ru-O(3) bond is the apical bond which points predominantly along c , while Ru-O(1) and Ru-O(2) are the basal bonds predominantly in the ab plane. The distortion angles are the tilt Θ , the angle between the Ru-O(3) bond and the c axis, and rotation Φ , which measures the angle between the Ru-O(2) basal bond and the [110] direction.

The octahedral structures are, again, very sensitive to temperature. The ambient pressure measurements by Porter [34]

and Steffens [3] at 90 and 295 K, respectively, are both included in Figs. 5(b)–5(g) (open vs closed symbols). Both measure the *S-Pbca* phase. At room temperature the apical bond is *longer* than the basal bonds (elongated octahedra), but at low temperatures it is *shorter* (compressed octahedra). The latter agrees well with our ground state calculations, where the insulating phase is associated with axially compressed octahedra and all metallic phases are axially elongated—in concert with the *c*-axis behavior (Fig. 4). HMe1 and HMe2 (seen for $U = 1.25$ eV, $P > 5$ GPa) have very similar octahedral structures, but the fully metallic phase ($U = 0.0$ eV, $P > 8$ GPa) shows the best agreement with experiment (albeit at a higher pressure).

The distortion angle Θ decreases significantly with temperature, while Φ is found to be quite insensitive to temperature [34]; note that the magnitude of Φ reported in [34] at room temperature disagrees somewhat with previous measurements [3]. Our results for Φ agree with the low temperature data at ambient pressure and with reported small increases under pressure in the metallic phases. Steffens' room temperature measurements of Θ show a sudden drop at the insulator-metal transition, followed by a steep decline towards 0° . Our results reproduce the drop at the transition, but show a much slower reduction of Θ with pressure. This is likely to be a signal of the higher-symmetry *Bbcm* phase emerging in the room temperature experiment. We will discuss the emergence of this phase in more detail in Sec. II E.

D. Orbital structure under pressure

We now probe the occupancies of the Ru *4d* orbitals to characterize the electronic behavior alongside the pressure induced structural changes. The Ru atom at the origin is chosen for our analysis [Fig. 5(a)], to which all other Ru sites are equivalent via appropriate symmetry operations [19]. For the basis set to be appropriate, the *z* axis for the orbital projection is chosen along the apical bond. The *x* axis is then chosen such that the Ru-O(1) bond is in the *xz* plane, which then fully determines the *y* axis. In practice, the Ru-O bonds are always within 5° of these cartesian axes. Occupancies are computed by integrating over the valence space of the ℓm resolved DOS, from -10 eV to the Fermi energy. The partial DOS in turn is obtained by projecting all electronic states onto spherical harmonics within a fixed radius around the Ru site. Absolute occupancies should therefore be treated with caution but relative changes and trends across pressure and phase transitions will be identifiable. Figure 6 shows the total orbital occupancies for the three exemplar U discussed above, in addition to the majority (up) and minority (down) spin channels.

The majority spin channel is remarkably robust across the insulating *S-Pbca* and both HMe phases, with archetypal splitting between e_g and t_{2g} orbitals. The residual occupancies of the e_g states (about 0.3 in both d_{z^2} and $d_{x^2-y^2}$) reflect the numerical limitations of the DOS projection scheme of a DFT band structure. The insulator-metal transition has no impact on the up-spin occupancies (see $U = 1.25$ and 1.75 eV) but is clearly noticeable in the minority spin state occupancies. For all metallic phases the total occupancy of the t_{2g} states

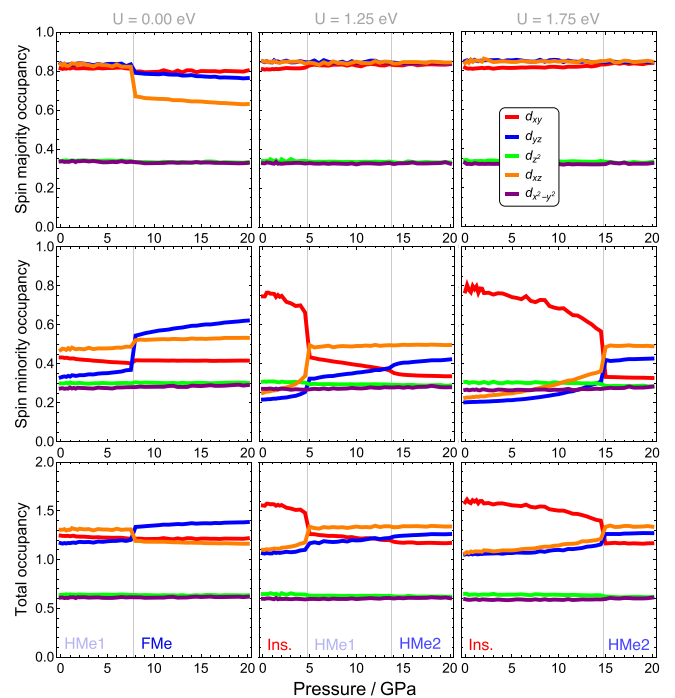


FIG. 6. Ru *4d* orbital occupancies for $U = 0.0, 1.25,$ and 1.75 eV as a function of pressure. Top: Majority spin channel (up spins). Middle: Minority spin channel (down spins). Bottom: Total orbital occupancies (up + down). Vertical lines mark phase transitions.

is approximately 1.25, consistent with DMFT results of 4/3 [16,18]. In the insulating phase only the d_{xy} orbital is doubly occupied while d_{xz} and d_{yz} are half occupied, also consistent with DMFT results. Electronic charge is localized in the basal plane of the octahedra, which correlates with the compressed octahedral shape. However, close to the insulator-metal transition, but still within the *S-Pbca* phase, charge density is redistributed into the d_{yz} and d_{xz} orbitals that are extended along the apical bond, correlating with reduction of the octahedral compression, and the anomalous *c* lattice expansion under pressure.

The occupancies change somewhat differently in the different half-metallic phases. HMe1 retains some charge density in the d_{xy} orbital, which is steadily shifted into the d_{yz} orbital as pressure increases. HMe2 is qualitatively the same, but the d_{xy} occupancy is lower and eclipsed by the d_{yz} orbital occupancy from the onset of metallicity. The crossover from d_{xy} to d_{yz} , and resulting charge transfer from the basal plane to the apical direction, correlates with the weak *c* lattice expansion seen in the half-metallic phases (see Fig. 4).

Finally, in the FMe phase, the majority spin channel loses charge density, primarily from the d_{xz} orbital, to the d_{yz} orbital in the minority spin channel. The charge density remains distributed largely along the apical bond, but with more substantial double occupancy of the d_{yz} orbital, hence the reduction in overall magnetic moment μ_B . This has little consequence for the total occupancy; the orbital polarization remains small.

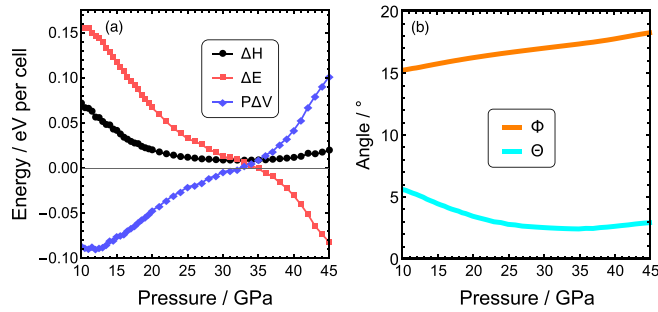


FIG. 7. (a) Enthalpy, energy, and pressure-volume differences between the *Bbcm* and FMe *L-Pbca* phases as a function of pressure. $\Delta X = X_{Bbcm} - X_{Pbca}$. (b) Octahedral distortion angles of the FMe *L-Pbca* phase under high pressure. See Fig. 5(a) for definitions of Θ (tilt) and Φ (rotation).

E. *L-Pbca* \rightarrow *Bbcm* transition

At atmospheric pressure Ca_2RuO_4 undergoes a phase transition to a higher symmetry *Bbcm* structure at 650 K, which is characterized by a vanishing tilt angle (octahedra aligning along the *c* axis). This type of phase transition is typical of compounds with polyhedral structures, where the high symmetry phase is dynamically stabilized by thermal fluctuations in the tilt angle [43]. Steffens *et al.* showed that, at 295 K, this transition appears at 5.5 GPa [3], indicating that pressure also acts to stabilize this phase. Here we probe the pressure dependence of the *Bbcm* phase up to much higher pressures to determine its static stability relative to the *L-Pbca* phase. We use $U = 0.0$ eV since the pressures here are more extreme.

The *L-Pbca* and *Bbcm* structures are independently pressurized up to 45 GPa. One expects that the *L-Pbca* phase converges to the *Bbcm* structure as the octahedral tilt is suppressed by pressure. However, both structures remain distinct and *L-Pbca* remains the lower-enthalpy phase over the full pressure range tested, see Fig. 7(a). The enthalpy difference decreases to a minimum of $\Delta H = 2.1$ meV/Ru at 33 GPa, before increasing again with further compression. The tilt angle follows the same trend, so that *Bbcm* symmetry (where $\Phi = 0$) is never reached, see Fig. 7(b). This behavior is driven by deformation of the octahedra in the *L-Pbca* phase (see the SM for details [27]) and suggests that this second-order phase transition line never meets the $T = 0$ axis. However, perovskite-type compounds are known to undergo a variety of structural phase transitions under extreme compression [44,45], which might be the case for Ca_2RuO_4 as well but was not considered in this work.

III. CONCLUSIONS

In summary, we have studied the high pressure evolution of the structural and electronic properties of Ca_2RuO_4 using DFT and DFT+ U calculations. Despite being conceptually very simple, the full structural optimizations (and therefore truly self-consistent electronic structures) are able to describe many of the interesting features seen in experiments, provided the on-site correction U is chosen appropriately. Namely, this includes the association of a short (S) crystal structure with an insulating band structure, and a long (L) crystal structure with a metallic band structure. Pressure-driven insulator-metal transitions also appear naturally, which coincides with a transition from S to L crystal structures. Generally, lattice parameters agree well with low temperature experimental measurements, but a full theoretical picture is complicated by the appearance of three metallic phases as a function of pressure: two half-metallic (HMe), local-moment phases, and a fully metallic (FMe) itinerant magnet which best matches the experimental *L-Pbca* phase. The Fermi surface of the FMe phase is also, geometrically, very well nested, suggesting that density-wave order may play a role in the phase diagram of Ca_2RuO_4 .

The Mott transition is a simultaneous restructuring of both crystal and orbital structure. Pressure squeezes electrons out of the basal d_{xy} orbital and into the d_{yz} and d_{xz} orbitals. The crystal structure responds by extending the apical bond of the octahedra and in turn, the *c* axis. This is generally in agreement with the previous DMFT study of the temperature driven transition [18]. The *Pbca* \rightarrow *Bbcm* transition is also probed to much higher pressures, which reveals that *Bbcm* never becomes the enthalpically stable phase at sufficiently low temperature. A high pressure, post-perovskite-type phase is likely to take its place. Hence, the low-temperature, high-pressure region of the Ca_2RuO_4 phase diagram remains a promising refuge for exotic structural, electronic, and magnetic phases.

ACKNOWLEDGMENTS

H.D.J.K. acknowledges studentship funding from EPSRC under Grant No. EP/L015110/1. Computing resources provided in parts by the UK national high performance computing service, ARCHER, and the UK Materials and Molecular Modelling Hub, which is partially funded by EPSRC (EP/P020194), and for which access was obtained via the UKCP consortium funded by EPSRC Grant No. EP/P022561/1, are gratefully acknowledged. S.R.J. is grateful to NSERC for funding (RGPIN-2019-06446), and to Andrew Huxley and the University of Edinburgh for hosting a sabbatical visit.

- [1] S. Nakatsuji, S. Ikeda, and Y. Maeno, Ca_2RuO_4 : New Mott insulators of layered ruthenate, *J. Phys. Soc. Jpn.* **66**, 1868 (1997).
 [2] F. Nakamura, T. Goko, M. Ito, T. Fujita, S. Nakatsuji, H. Fukazawa, Y. Maeno, P. Alireza, D. Forsythe, and S. R. Julian, From Mott insulator to ferromagnetic metal: A pressure study of Ca_2RuO_4 , *Phys. Rev. B* **65**, 220402(R) (2002).

- [3] P. Steffens, O. Friedt, P. Alireza, W. G. Marshall, W. Schmidt, F. Nakamura, S. Nakatsuji, Y. Maeno, R. Lengsdorf, M. M. Abd-Elmeguid, and M. Braden, High-pressure diffraction studies on Ca_2RuO_4 , *Phys. Rev. B* **72**, 094104 (2005).
 [4] Y. Maeno, H. Hashimoto, K. Yoshida, S. Nishizaki, T. Fujita, J. G. Bednorz, and F. Lichtenberg, Superconductivity in a

- layered perovskite without copper, *Nature (London)* **372**, 532 (1994).
- [5] S. Nakatsuji and Y. Maeno, Quasi-Two-Dimensional Mott Transition System $\text{Ca}_{2-x}\text{Sr}_x\text{RuO}_4$, *Phys. Rev. Lett.* **84**, 2666 (2000).
- [6] P. L. Alireza, F. Nakamura, S. K. Goh, Y. Maeno, S. Nakatsuji, Y. T. C. Ko, M. Sutherland, S. Julian, and G. G. Lonzarich, Evidence of superconductivity on the border of quasi-2D ferromagnetism in Ca_2RuO_4 at high pressure, *J. Phys. Condens. Matter* **22**, 052202 (2010).
- [7] F. Nakamura, M. Sakaki, Y. Yamanaka, S. Tamaru, T. Suzuki, and Y. Maeno, Electric-field-induced metal maintained by current of the Mott insulator Ca_2RuO_4 , *Sci. Rep.* **3**, 2536 (2013).
- [8] K. Takenaka, Y. Okamoto, T. Shinoda, N. Katayama, and Y. Sakai, Colossal negative thermal expansion in reduced layered ruthenate, *Nat. Commun.* **8**, 14102 (2017).
- [9] D. Chen, A. Jain, B. Kim, G. Khaliullin, G. Ryu, M. Krautloher, D. Abernathy, A. Ivanov, B. Keimer, J. Chaloupka, J. Park, and J. Porras, Higgs mode and its decay in a two-dimensional antiferromagnet, *Nat. Phys.* **13**, 633 (2017).
- [10] H. Taniguchi, K. Nishimura, R. Ishikawa, S. Yonezawa, S. K. Goh, F. Nakamura, and Y. Maeno, Anisotropic uniaxial pressure response of the Mott insulator Ca_2RuO_4 , *Phys. Rev. B* **88**, 205111 (2013).
- [11] S. Riccò, M. Kim, A. Tamai, S. McKeown Walker, F. Y. Bruno, I. Cucchi, E. Cappelli, C. Besnard, T. K. Kim, P. Dudin, M. Hoesch, M. J. Gutmann, A. Georges, R. S. Perry, and F. Baumberger, *In situ* strain tuning of the metal-insulator-transition of Ca_2RuO_4 in angle-resolved photoemission experiments, *Nat. Commun.* **9**, 4535 (2018).
- [12] L. Woods, Electronic structure of Ca_2RuO_4 : A comparison with the electronic structures of other ruthenates, *Phys. Rev. B* **62**, 7833 (2000).
- [13] Z. Fang and K. Terakura, Magnetic phase diagram of $\text{Ca}_{2-x}\text{Sr}_x\text{RuO}_4$ governed by structural distortions, *Phys. Rev. B* **64**, 020509(R) (2001).
- [14] V. Anisimov, I. Nekrasov, D. Kondakov, T. Rice, and M. Sigrist, Orbital-selective Mott-insulator transition in $\text{Ca}_{2-x}\text{Sr}_x\text{RuO}_4$, *Eur. Phys. J. B* **25**, 191 (2002).
- [15] J. H. Jung, Z. Fang, J. P. He, Y. Kaneko, Y. Okimoto, and Y. Tokura, Change of Electronic Structure in Ca_2RuO_4 Induced by Orbital Ordering, *Phys. Rev. Lett.* **91**, 056403 (2003).
- [16] A. Liebsch and H. Ishida, Subband Filling and Mott Transition in $\text{Ca}_{2-x}\text{Sr}_x\text{RuO}_4$, *Phys. Rev. Lett.* **98**, 216403 (2007).
- [17] G. Liu, Spin-orbit coupling induced Mott transition in $\text{Ca}_{2-x}\text{Sr}_x\text{RuO}_4$ ($0 \leq x \leq 0.2$), *Phys. Rev. B* **84**, 235136 (2011).
- [18] E. Gorelov, M. Karolak, T. O. Wehling, F. Lechermann, A. I. Lichtenstein, and E. Pavarini, Nature of the Mott Transition in Ca_2RuO_4 , *Phys. Rev. Lett.* **104**, 226401 (2010).
- [19] G. Zhang and E. Pavarini, Mott transition, spin-orbit effects, and magnetism in Ca_2RuO_4 , *Phys. Rev. B* **95**, 075145 (2017).
- [20] Q. Han and A. Millis, Lattice Energetics and Correlation-Driven Metal-Insulator Transitions: The Case of Ca_2RuO_4 , *Phys. Rev. Lett.* **121**, 067601 (2018).
- [21] H. Hao, A. Georges, A. J. Millis, B. Rubenstein, Q. Han, and H. Shi, Metal-insulator and magnetic phase diagram of Ca_2RuO_4 from auxiliary field quantum Monte Carlo and dynamical mean field theory, *Phys. Rev. B* **101**, 235110 (2020).
- [22] G. Kresse and J. Furthmüller, Efficient iterative schemes for *ab initio* total-energy calculations using a plane-wave basis set, *Phys. Rev. B* **54**, 11169 (1996).
- [23] J. P. Perdew, K. Burke, and M. Ernzerhof, Generalized Gradient Approximation Made Simple, *Phys. Rev. Lett.* **77**, 3865 (1996).
- [24] G. Kresse and D. Joubert, From ultrasoft pseudopotentials to the projector augmented-wave method, *Phys. Rev. B* **59**, 1758 (1999).
- [25] J. P. Perdew and A. Zunger, Self-interaction correction to density-functional approximations for many-electron systems, *Phys. Rev. B* **23**, 5048 (1981).
- [26] J. Sun, A. Ruzsinszky, and J. P. Perdew, Strongly Constrained and Appropriately Normed Semilocal Density Functional, *Phys. Rev. Lett.* **115**, 036402 (2015).
- [27] See the Supplemental Material at <http://link.aps.org/supplemental/10.1103/PhysRevB.104.085143> for effects of exchange-correlation functionals, spin-orbit coupling, magnetic settings, and for structural details of the *Bbcm* phase [28–31].
- [28] J. W. Furness, Y. Zhang, C. Lane, I. G. Buda, B. Barbiellini, R. S. Markiewicz, A. Bansil, and J. Sun, An accurate first-principles treatment of doping-dependent electronic structure of high-temperature cuprate superconductors, *Commun. Phys.* **1**, 11 (2018).
- [29] C. Lane, J. W. Furness, I. G. Buda, Y. Zhang, R. S. Markiewicz, B. Barbiellini, J. Sun, and A. Bansil, Antiferromagnetic ground state of La_2CuO_4 : A parameter-free *ab initio* description, *Phys. Rev. B* **98**, 125140 (2018).
- [30] J. Varignon, M. Bibes, and A. Zunger, Mott gapping in $3d\text{ABO}_3$ perovskites without Mott-Hubbard interelectronic repulsion energy U , *Phys. Rev. B* **100**, 035119 (2019).
- [31] H. Peng and J. P. Perdew, Synergy of van der Waals and self-interaction corrections in transition metal monoxides, *Phys. Rev. B* **96**, 100101(R) (2017).
- [32] B. Himmetoglu, A. Floris, S. Gironcoli, and M. Cococcioni, Hubbard-corrected DFT energy functionals: The LDA+U description of correlated systems, *Int. J. Quantum Chem.* **114**, 14 (2014).
- [33] S. L. Dudarev, G. A. Botton, S. Y. Savrasov, C. J. Humphreys, and A. P. Sutton, Electron-energy-loss spectra and the structural stability of nickel oxide: An LSDA+ U study, *Phys. Rev. B* **57**, 1505 (1998).
- [34] D. G. Porter, V. Granata, F. Forte, S. Di Matteo, M. Cuoco, R. Fittipaldi, A. Vecchione, and A. Bombardi, Magnetic anisotropy and orbital ordering in Ca_2RuO_4 , *Phys. Rev. B* **98**, 125142 (2018).
- [35] A. M. Glazer, The classification of tilted octahedra in perovskites, *Acta Crystallogr. Sect. B* **28**, 3384 (1972).
- [36] P. M. Woodward, Octahedral tilting in perovskites. I. Geometrical considerations, *Acta Crystallogr. Sect. B* **53**, 32 (1997).
- [37] C. J. Howard and H. T. Stokes, Group-theoretical analysis of octahedral tilting in perovskites, *Acta Crystallogr. Sect. B* **54**, 782 (1998).
- [38] S. Lee, J. R. Zhang, S. Torii, S. Choi, D.-Y. Cho, T. Kamiyama, J. Yu, K. A. McEwen, and J.-G. Park, Large in-plane deformation of RuO_6 octahedron and ferromagnetism of bulk SrRuO_3 , *J. Phys. Condens. Matter* **25**, 465601 (2013).
- [39] S. Middey, J. Chakhalian, P. Mahadevan, J. Freeland, A. Millis, and D. Sarma, Physics of ultrathin films and heterostructures of rare-earth nickelates, *Annu. Rev. Mater. Res.* **46**, 305 (2016).
- [40] A. Mercy, J. Bieder, J. Íñiguez, and P. Ghosez, Structurally triggered metal-insulator transition in rare-earth nickelates, *Nat. Commun.* **8**, 1677 (2017).

- [41] J. Varignon, M. Bibes, and A. Zunger, Origin of band gaps in $3d$ perovskite oxides, *Nat. Commun.* **10**, 1658 (2019).
- [42] O. E. Peil, A. Hampel, C. Ederer, and A. Georges, Mechanism and control parameters of the coupled structural and metal-insulator transition in nickelates, *Phys. Rev. B* **99**, 245127 (2019).
- [43] S. A. T. Redfern, High-temperature structural phase transitions in perovskite, *J. Phys. Condens. Matter* **8**, 8267 (1996).
- [44] H. Kojitani, Y. Shirako, and M. Akaogi, Post-perovskite phase transition in CaRuO_3 , *Phys. Earth Planet. Inter.* **165**, 127 (2007).
- [45] M. Murakami, K. Hirose, K. Kawamura, N. Sata, and Y. Ohishi, Post-perovskite phase transition in MgSiO_3 , *Science* **304**, 855 (2004).